university of groningen

faculty of science and engineering

Readout optimization of Silicon Photomultiplier arrays for neutron detection

Author:
Eduard CORGHENCEA
(S4794583)

Supervisor:
dr. M. KAVATSYUK
Second examiner :
prof. R. HOEKSTRA

Bachelor's Thesis
To fulfill the requirements for the degree of
Bachelor of Science in Applied Physics
at the University of Groningen

July 13, 2024

Contents

Abstract

Silicon Photomultipliers (SiPMs) are a relatively new multi-pixel technology intended for nuclear and particle physics uses. They consist of a silicon substrate onto which multiple Single Photon Avalanche Diodes (SPADs) are connected to a quenching resistor, which forms one of the pixels. These pixels are connected in parallel, which result in a well defined signal. The use of SiPMs in arrays, such as series, parallel or mixed can prove useful in constructing a vacuum-friendly detector that is unaffected by magnetic fields. The parallel SiPM configuration, composed of two Hamamatsu S13360-6050CS SiPMs is studied. The optimal parameters of the experimental setup are researched and discussed. A table of Relative Energy Resolutions is given, containing data from the original sampling rate of 2 GHz, as well as data from simulated 1 GHz, 500 MHz, 250 MHz and 125 MHz devices.

Acknowledgments

Over a period of 3 months of extensive research, the project came slowly but surely to fruition. This is thanks to Dr. Myroslav Kavatsyuk, whose guidance and expertise I wish for everybody to experience. This project will (hopefully) serve well for the scientific community and for the greater goal of achieving a revolutionary neutron detection device.
It is also important to mention the collective at the Kernfysisch Versneller Instituut (KVI). Through the constant feedback, discussion and laughs shared throughout the meetings and the research period, I managed to gather the courage to get this project to an end.

1 Introduction

1.1 Background and Motivation

Neutron detection and spectra imaging play a critical role in various fields, including nuclear physics, homeland security, and medical diagnostics. Traditional neutron detectors often rely on photomultiplier tubes (PMTs), which, despite their widespread use and high sensitivity, present several challenges such as bulkiness, sensitivity to magnetic fields, and amplification of all present radiation noise. Silicon photomultipliers (SiPMs) have emerged as a recent and promising alternative, with efficiencies similar to PMTs. At the same time, they offer distinct advantages in terms of compactness, operating voltage and insensitivity to magnetic fields [1].

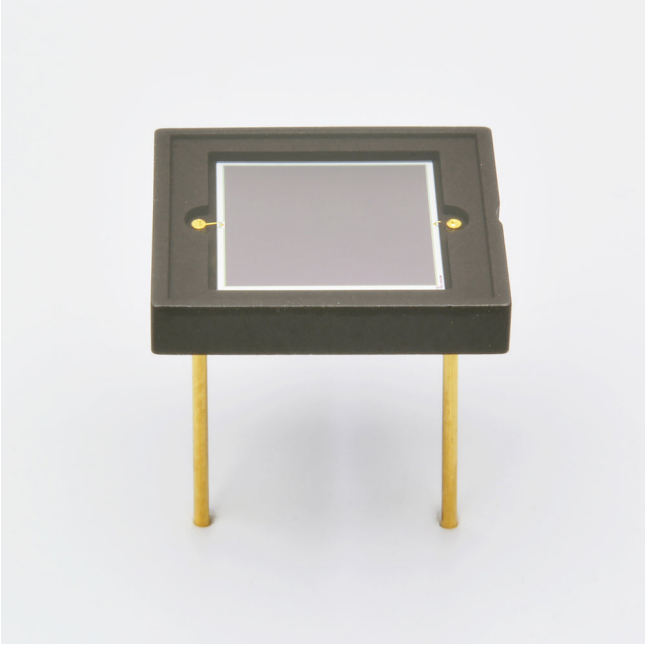

Figure 1: Hamamatsu S13360-6050CS used in the experiment [2]

SiPMs are semiconductor devices composed of an array of micropixels operating in Geiger mode. These micropixels can detect single photons and provide high gain, making them suitable for various applications in photon detection and neutron spectroscopy [1][3]. Unlike PMTs which operate at 300V-1500V, SiPMs operate at a voltage of around 55V. The SiPMs lack the voltage divider component that is present in PMTs. This allows SiPMs to be operated in vacuum, where measuring neutron scattering is significantly easier due to a lack of air, which would introduce extra scattering for the neutrons. SiPMs are also more mechanically robust, with operation surfaces on the order of mm^2, which simplifies their integration into portable and compact detection systems [1]. Additionally, SiPMs offer a higher single photon detection efficiency (PDE) across a broader range of wavelengths, as opposed to PMTs which are more limited for single wavelengths [1].

Despite these advantages, SiPMs are not without their drawbacks. The main disadvantages are the dark count rate (DCR) and the weak gain dependence on temperature [1]. Furthermore, the dynamic range of SiPMs is limited by the number of micropixels, with a theoretical technological upper limit of $(2-3)*10^3 mm^{-2}$ [1]. These limitations suggest that study and improvements of SiPM-based

neutron detectors are necessary.

To address these challenges, this paper explores the possibilities of optimization of SiPM readouts for neutron detectors. Specifically, various detector configurations are investigated. SiPM parallel, series, and mixed configurations are promising candidates for study using a LED pulser.

One of the main characteristics of particle detectors that is studied is the energy resolution. Energy resolution is crucial for accurately identifying and quantifying particle interactions through the identified energy ranges. Various SiPM configurations can influence factors such as gain uniformity, noise reduction, and photon detection efficiency. For example, connecting SiPMs in parallel can increase the dynamic range, while series configurations might improve the signal-to-noise ratio due to a higher breakdown voltage.

Another detector type that might be useful for study is the digital SiPM, which overcomes some challenges of the normal detectors, such as parasitic capacitance [4].

The following chapters will detail the methodology used to test and evaluate the parallel SiPM configuration, present experimental results, and discuss the implications of these findings. This research aims to further the area of Silicon-based radiation detectors and to explore the possibilities of improvement. This, in turn, will contribute to the development of more efficient, compact, and accurate radiation detection systems, which are essential for advancements in various scientific and industrial applications. Through a study of the parallel SiPM configuration, the paper examines the current limitations and proposes possibilities for future innovations in the field of radiation detection.

1.2 Problem Definition

With the comparison made between PMTs and SiPMs, it becomes clear that a vacuum-friendly neutron measuring device can be achieved through the use of SiPMs. This would help reduce neutron scattering in air and would allow for less residual heat as there is no voltage divider element present.

To be able to properly and efficiently construct such a device, a characterisation of the optimal parameters of the hardware and software components is needed. The elements that make up the hardware and software part are shown in figure 2.

As such, this study aims to highlight and discuss the key parameters involved in the operation of a detector based on a parallel SiPM arrays in conjunction with a preamplifier, digitizer, LED Pulser and a Python Data Processing program. The optimal relative energy resolution can be found in this way. The necessity of this research arises from a need to update the currently known neutron scattering interactions in nuclear databases with more accurate data.

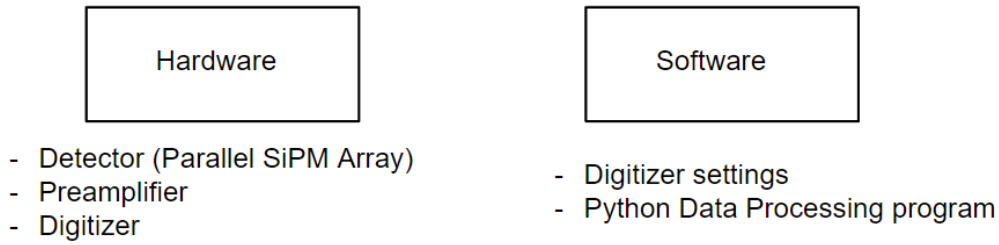

Figure 2: Setup Hardware and Software components

2 Theory

2.1 Neutron Detection

Understanding the theoretical background is essential for grasping the experimental motivations and methods in neutron detection. Generally, particle detection in high-energy physics is realized using detectors that rely on photon emissions with energies proportional to the incoming radiation. The proportionality is determined by the type of detector or configuration used to detect the relevant particles.

In nuclear physics, the traditional and well-known detection method is through the use of photomultiplier tubes (PMTs). PMTs operate based on an accelerated electron cascade understood through the Photoelectric effect. On the other hand, SiPMs operate in Geiger mode, where a single photon induces an avalanche of electrons, resulting in a detectable electrical signal.

Silicon detectors, in general, are widely used in particle physics experiments due to their excellent energy resolution capabilities. They operate based on the ionization of silicon atoms by charged particles, creating electron-hole pairs. The generated charge carriers (electrons and holes) drift towards the electrodes, producing a measurable electrical signal. Silicon detectors come in various forms, including silicon strip detectors, pixel detectors, and SiPMs [5].

2.2 SiPM Operational Principles

SiPMs, also known as multi-pixel photon counters, consist of many Geiger-mode avalanche photodiodes (APDs), called Single Photon Avalanche Diodes (SPAD) connected in parallel. Thanks to the multiple Single Photon Avalanche Diodes connected in parallel as shown in figure 3, the SiPM has intrinsic gain on the order of 10^6. These diodes are all kept at a bias voltage close to breakdown voltage which enables a proper operation. They operate by the formation of electron-hole pairs when a photon strikes the silicon. This interaction initiates an avalanche breakdown within the microcells of the SiPM, producing a cumulative electrical signal.

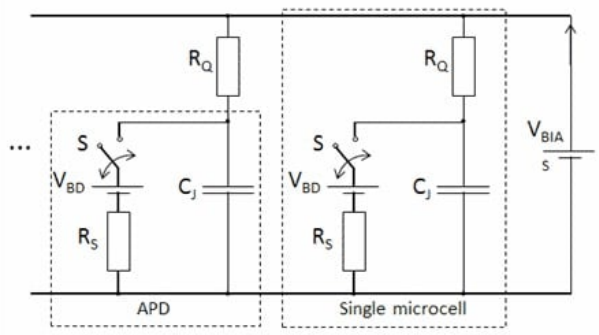

Figure 3: Internal Schematic of SiPM [2]

The microcells within SiPMs have 10ns recovery time [5], allowing for nearly proportional responses to light if the probability of multiple photon hits within a cell's recovery time is negligible.

Another essential component is the quenching resistor. Each microcell is equipped with a quenching resistor that stops the avalanche process, allowing the pixel to reset and be ready for the next photon detection. The resistor is essential in controlling the signal strength.

When SiPMs are exposed to light, the incident photons generate electron-hole pairs in the material. Each photon has a certain probability of triggering an avalanche breakdown in the Geiger-mode microcells of the SiPM.

In an ideal scenario, such as perfect energy resolution each detected photon results in a distinct pulse from the SiPM. The total output signal of the SiPM is a sum of these individual pulses.

The mean number of detected photons is proportional to the incident light intensity and the detection efficiency of the SiPM. As the intensity of the light increases, the mean number of detected photons increases, leading to a higher overall output signal.

2.3 Moving average and Nyquist Theorem

One technique applied in signal processing is that of a moving average. A moving average is a technique in which short-term fluctuations are smoothed out, while long-term trends are preserved. This is done by averaging a certain ”window” or number of points along the studied signal. This is done in order to reduce noise.

A moving average filter can be used for other purposes as well. Another use is in downsampling a signal. Combined with the Nyquist-Shannon sampling theorem, a signal can be fully represented and simulated by a lower amount of points, as long as the sampling rate is at least twice the maximum frequency. If this condition is not respected, aliasing occurs in the data which distorts the signal. In order to simulate a signal captured at a lower sampling rate, it is necessary to apply a moving average filter of 2 points, after which every 2nd point is removed. Proceeding in this way, the signal would be simulated as if captured by a device that has exactly half the sampling rate of the original device.

2.4 Amplifier

It is important to consider the theoretical aspect of amplifiers as well. According to Seifert(2009), there exists a certain parasitic effect due to the resistor and capacitor components. This parasitic RC in the amplifier can affect the signal output. The electronic signal may not be proportional to the number of fired cells if the amplifier input impedance is not zero. Lower parasitic capacitance increases the importance of the input impedance effect [6].

2.5 Statistical background

For photon counting devices, such as the SiPM, there is a close relationship between the physical phenomena present and Poisson distributions. Poisson distributions occurs in the case of discrete independent random events. In the case of SiPMs, due to the photon counting, the measured signal will be directly proportional to number of counts.

A Poisson distribution has the form:

$$P(k;\lambda) = \frac{\lambda^k e^{-\lambda}}{k!} \tag{1}$$

where $P(k;\lambda)$ is the probability of detecting k photons and λ is the mean number of photons detected. The variance of such a distribution is the same as the expectation value of the measured quantity, or equivalently: $\lambda = E[X] = Var(X)$.

In the limit of high number of discrete events, the Poisson distribution becomes approximately symmetric and can be replaced by a Gaussian distribution. In this case, the parameters become:
$\lambda \to \mu$ and the variance is $\sigma^2 = \mu$.

The Gaussian distribution has the form:

$$g(x) = \frac{1}{\sigma\sqrt{2\pi}} e^{\frac{-(x-\mu)^2}{2\sigma^2}} \tag{2}$$

With μ the expected value of the distribution and σ^2 the variance of the distribution. A gaussian fit is an appropriate fit for determining the normal distribution of events in nuclear physics and particle physics generally. Another relevant parameter for the Gaussian distribution in the context of particle physics is the Full Width at Half Maximum (FWHM). This represents the width between the points at half the amplitude of the signal. For a Gaussian distribution this can be calculated as:

$$FWHM = 2\sqrt{2\ln 2}\sigma \tag{3}$$

Using the FWHM and the expected value of the distribution, one can obtain the relative energy resolution as:

$$E_{res}(\%) = \frac{FWHM}{\mu} * 100\% \tag{4}$$

The relative energy resolution is an essential parameter in the context of particle detection. It is used to characterize how well the detector can resolve the true energy of a particle. In an ideal scenario, the particle signal should be a type of sharp peak, similar to a delta function. In reality, these energies are scattered across a range, which can be fitted to a Gaussian function.

In the context of measuring particle energy, a deduction on the relationship between energy and the variance measured in the Gaussian can be made. Knowing that the measured quantity is the energy of a pulse of light:

$$\mu = E \tag{5}$$

and the variance therefore is, in theory:

$$\sigma = \sqrt{E} \tag{6}$$

In reality, there are additional effects that need to be accounted for, such as a constant offset or dark counts.
A proportionality relationship is used to account for the possible secondary effects that might affect the value of the variance and the mean. Further developing the relationship with addition of a constant α for the primary effect, C for the constant offset and a constant D for the dark counts:

$$\sigma \propto \alpha\sqrt{E} + C + D * E \tag{7}$$

Division by the energy E yields a relationship that includes the relative energy resolution:

$$E_{res} \propto \sigma/\mu \propto \sigma/E \propto \frac{\alpha}{\sqrt{E}} + \frac{C}{E} + D \tag{8}$$

3 Experimental Method

3.1 Experimental Setup

The experimental setup, as illustrated in Figure 4, consists of the following essential components: two parallel connected SiPMs, an LED Pulser, a preamplifier, an Acqiris DAQ acquisition device (Digitizer), and bias voltage supplies.

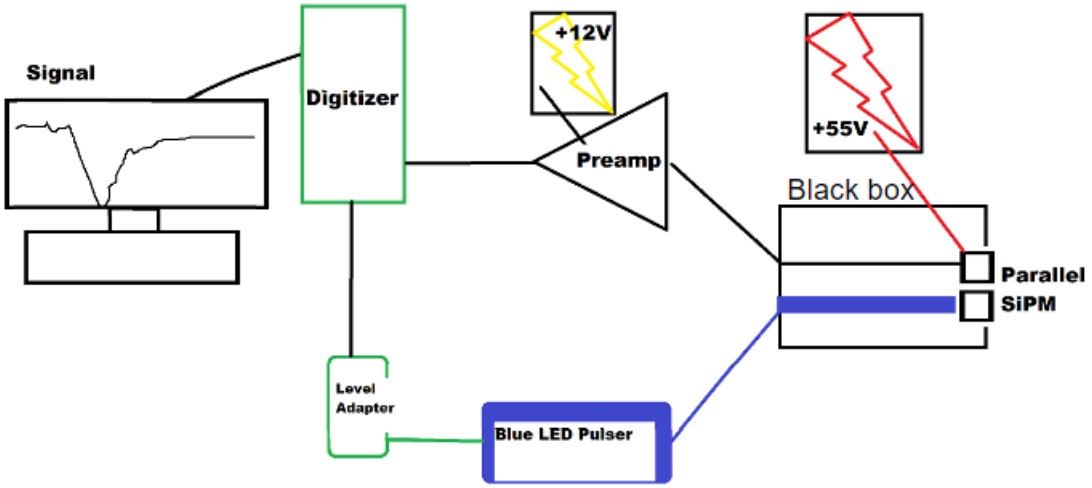

Figure 4: Experimental Setup

The specific SiPM model used is the Hamamatsu MPPC S13360-6050CS. Detailed specifications, including the active surface area, quantum efficiency and other parameters can be found in the product manual.

The Hamamatsu SiPM is housed in a black box to shield it from all external light sources due to its high sensitivity. The bias voltage of +55V is required to power the SiPM, this is just above the breakdown voltage for the Hamamatsu SiPM.Another +12V bias is used to power the preamplifier. The exact bias voltage depends on the specific SiPM model, the number of devices, and their configuration. For parallel configurations, the voltage remains the same as for a single cell, while for series configurations, the voltage is multiplied by the number of devices (e.g., for two SiPMs in series, the bias voltage is 2 * 55V = 110V).

The LED Pulser, though unmarked, allows adjustment of the emitted light amplitude from 0 to 10 and the pulse frequency. For this experiment, the frequency was set to 2 kHz. The LED Pulser also provides a logic signal that goes through the level adapter. This is used to accurately characterize the received pulse, with a trigger window size of approximately 50 ns.

The acquisition device is a MAQ Box from Acqiris, offering 4 channels with a sampling rate of up to 2 GSamples/s.

The preamplifier has 2 channels with an adjustable resistance element, which can be tuned using a screw. At one extreme, the waveform saturates faster with a higher voltage. This suggests that the

resistance is at a maximum. On the other extreme, the waveform exhibits strong oscillatory behaviour. For this experiment, the setting chosen was the one where the signal saturates faster, increasing the likelihood of observing single-cell events due to the higher signal amplitude.

The digitizer provides data in the HDF5 format, which typically requires specialized software to open. To process the acquisition data, the Python program mentioned in the previous section was used. A length of 750ns was chosen for all captured pulses, as this is enough to capture all important features. A moving average with a window of 50 points was chosen.

3.2 Python Data Processing

Efficient data processing methods are crucial for interpreting the signals from particle detectors. Digital filtering is required in order to properly analyze the signal and reduce the DC offset. The digital filtering is executed in the Python programming language through a program designed for the experimental setup, with the steps shown graphically in figure 5.

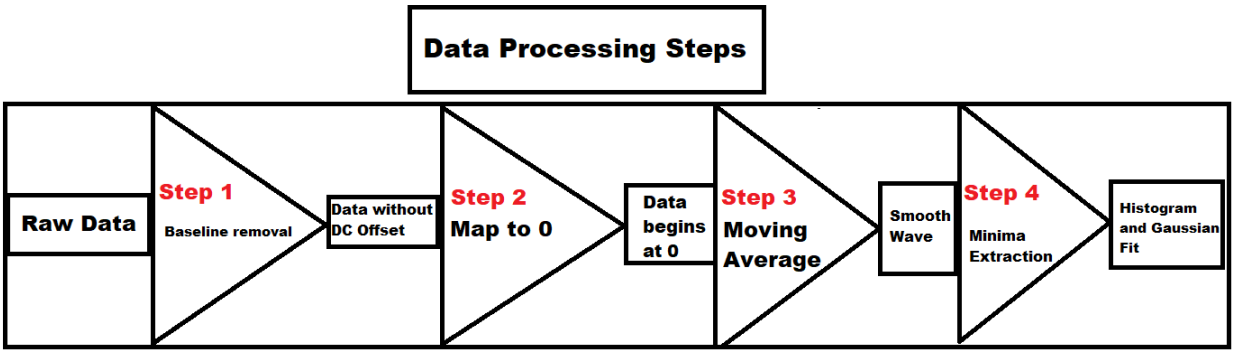

Figure 5: Data processing steps

The program extracts the data from the Acquisition device, after which the data is stored and processed through a couple of steps. A typical Raw waveform is shown in figure 6:

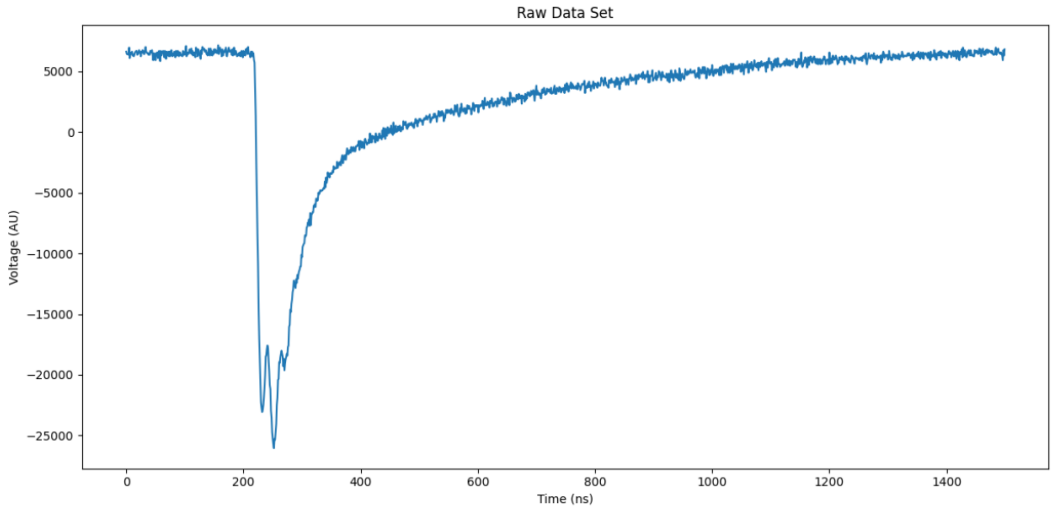

Figure 6: Typical Raw waveform (Step 0)

The first processing step is removal of the average of the waveform in order to get rid of the DC offset. This reduces the y-value of all points by a fixed amount. For this particular waveform, the step reduces the relatively flat beginning values from above 5000 units to under 5000 units in figure 7:

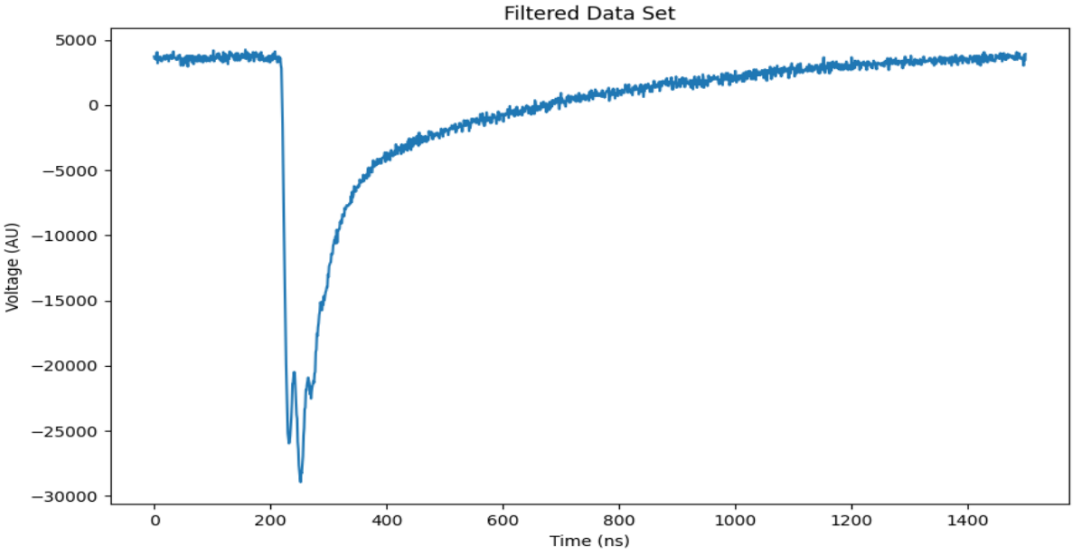

Figure 7: Waveform after baseline subtraction (Step 1)

Then an additional filter is applied in order to shift the baseline as close to 0 as possible. This is achieved by removing the value of the first point from data in order to vertically shift the whole waveform. This is shown in figure 8.

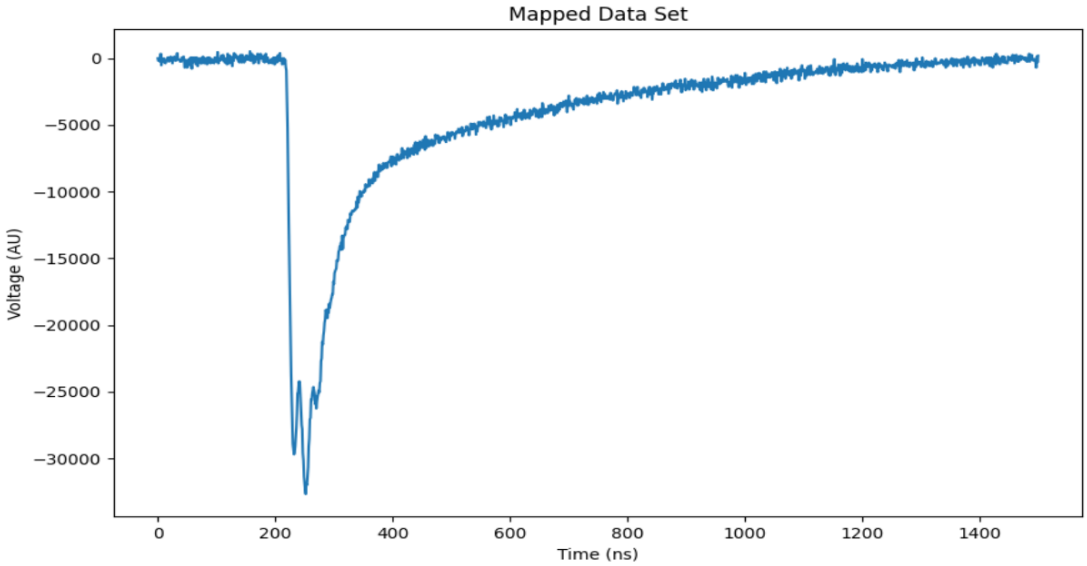

Figure 8: Waveform with the first point mapped to 0 (Step 2)

The filtered data is then averaged using a moving average of a 50 point window size. This is performed in order to smooth out the signal and reduce variations in the peak of the waveform. This is shown below in figure 9.

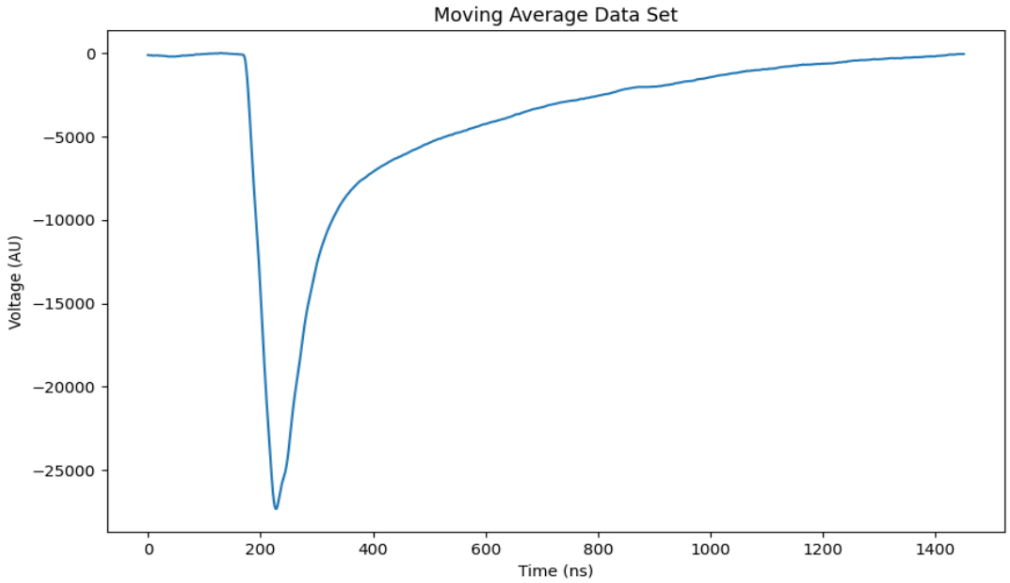

Figure 9: Smooth waveform after moving average filter (Step 3)

Finally, due to the negative value of the signal, the minima of the signal is then extracted and added to a histogram, onto which a Gaussian function is fitted. The final step is essential in characterizing the SiPM parallel array and the output of this step is shown in figure 10.

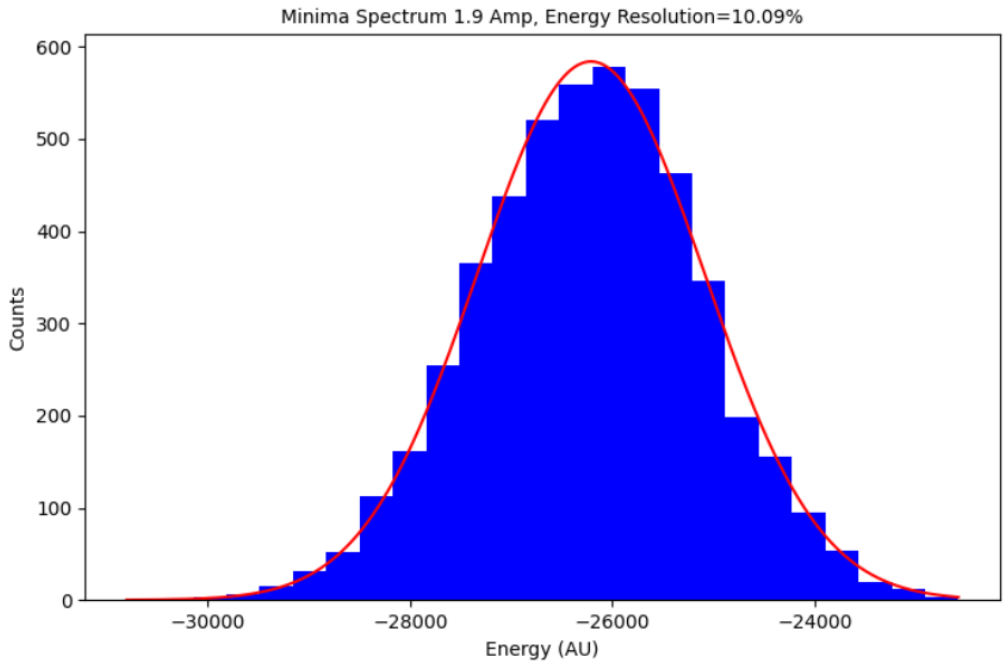

Figure 10: Histogram with fitted Gaussian (Step 4)

This allows for an extraction of the variance σ^2 and expected value μ of the histograms through the use of the Gaussian fits. The variance and expected value are used directly to calculate the relative energy resolution according to equation 4.

4 Results and Discussion

In this section, the parameters obtained for the hardware and software components of the experimental setup are presented.

Data was acquired over a range of intensities set from the LED Pulser. The results are showcased for low, middle and high intensities. The intensity range is based on the amplitude setting on the LED Pulser. The range starts from an intensity of 1.2, going all the way to 2.2, after which the pulse saturates. The range was chosen this way due to the possibility of obtaining differentiated single cell signals for low intensities, with the intermediary range serving the purpose of characterising the energy resolution of the parallel configuration. The time window of all measurements is 750 ns, with the y-axis representing the Voltage in arbitrary units (AU) for Raw and Filtered waveforms. For the histograms with the Gaussian fits, the x-axis is Energy in arbitrary units (AU) and the y-axis is the number of occurences or counts.

4.1 Preamplifier Settings

The first relevant result which helped determine further the optimal parameters of the setup were the preamplifier setting. The adjustable resistance screw element of the preamplifier offers an increase or decrease in the resistance. There are no markings, so the increase or decrease in the resistance would be observable based on the signal shape, as it varies drastically at the two ends. The first result is presented in figure 11. Note the strong oscillatory behaviour.

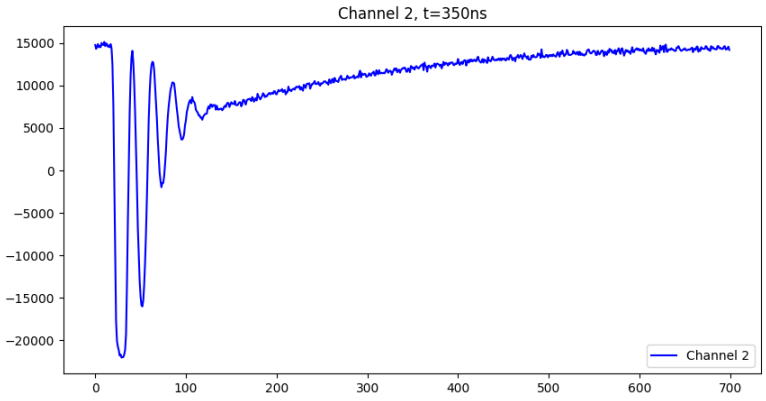

Figure 11: Capacitor-dominated signal

The other extreme is where the resistance is the lowest. This region is characterized by a strong signal that saturates fast relative to the other extreme. The signal in this region overshoots if the signal is saturated. A lack of oscillatory behaviour suggests that the capacitor has no influence at all over the shape of the signal. This extreme is shown below in figure 12.

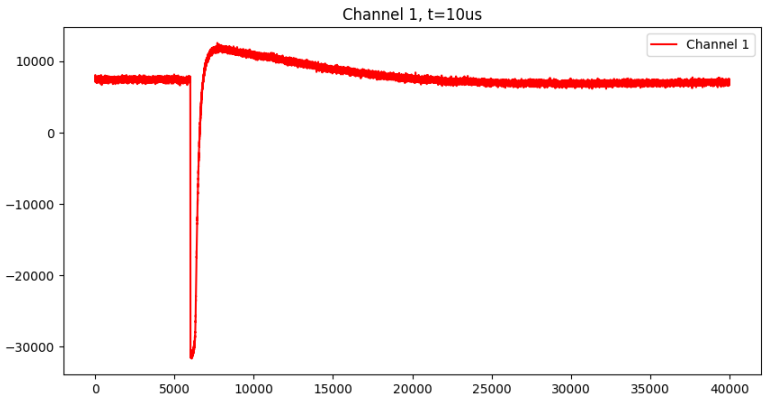

Figure 12: Resistor-dominated signal

The Resistor-dominated setting was chosen throughout the rest of the experiment. This regime yielded a better defined signal for lower intensities, which was preferable in order to observe and study the nature of the SiPM parallel array.

4.2 Parallel SiPM Array

4.2.1 Low Intensity

The waveforms obtained in the low intensity regime are dominated by noise due to the low signal strength. The characteristic of this regime are the presence of multiple peaks over the whole time range. The raw and filtered waveforms are shown in figure 13. The energy resolutions belonging to this mode are greater than 100%.

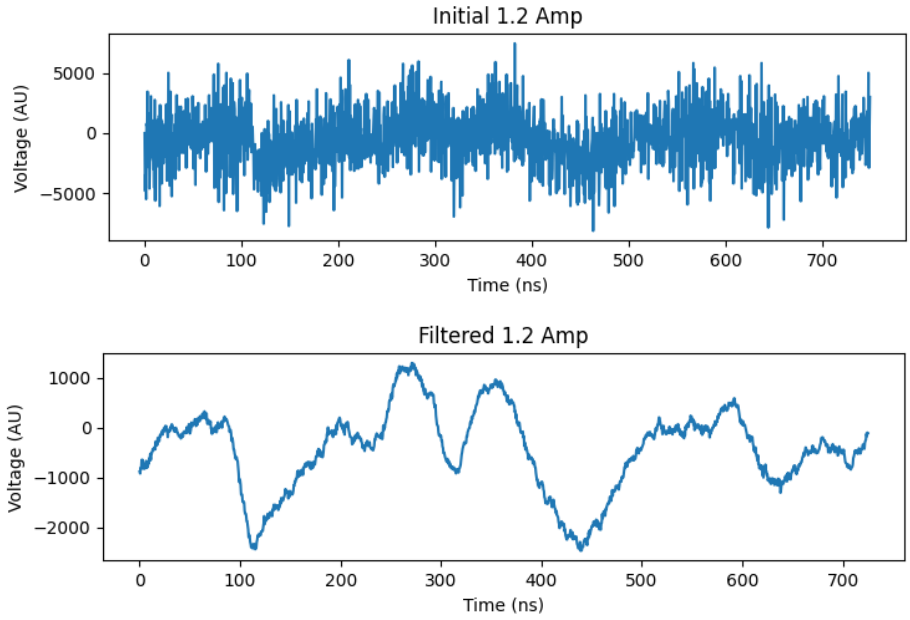

Figure 13: Raw and Filtered Waveform at 1.2 Intensity

Although the low intensity (1.2 to 1.45) signals are overwhelmed by noise, they are not without use.

They serve as visual indicators for the phenomenon of a multiple single Avalanche Photodiodes charging. This can be observed in figure 13. There are multiple peaks present over the range. The peaks are initially hard to distinguish in the raw signal, as the signal possesses a lot of noise. The filtering algorithm helps distinguish the individual peaks. The algorithm is not working fully as intended, this can be observed at the start of the signal. This is due to the variation in the signal being comparable to the peak of the signal.

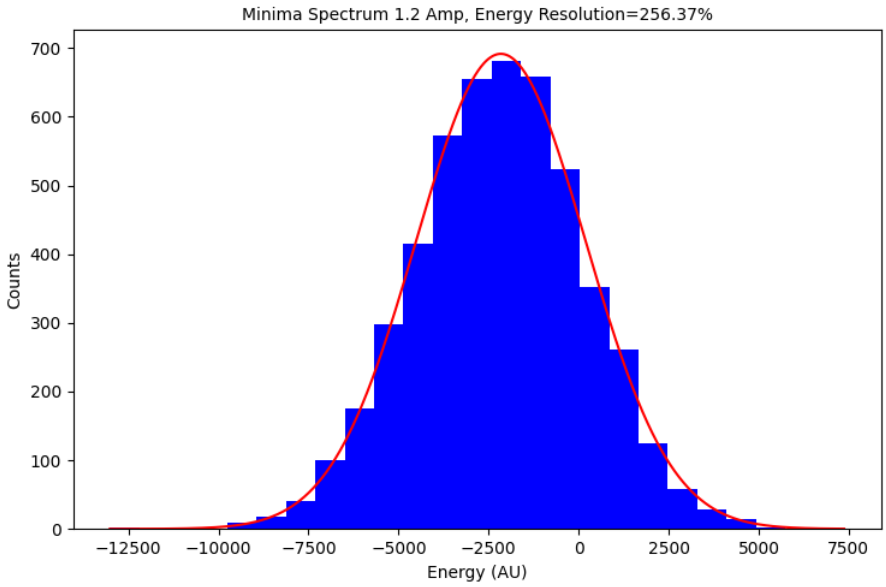

Figure 14: Gaussian Fit of 1.2 Intensity Spectrum

The energy resolution in this regime begins with a value of $E_{res} = 256.37\%$ at an intensity of 1.2. This is expected due to the algorithm not setting to 0 properly, the variance in the signal masking the peak and the Histogram crossing 0.

It is important to consider the low intensity case in a better controlled environment with a known energy source, such as a known radioactive sample. Further study of this regime is required to mathematically confirm the presence of the single-cell charging events. In an ideal scenario, the histogram should contain peaks with clearly defined separation, corresponding to a different integer number of cells charging. The wide range of the Gaussian plotted over the histogram in figure 14 might contain the aforementioned individual peaks, but due to the low intensity regime, their separation might be less than their variance, which would result in an overlap.

4.2.2 Intermediary Intensity

The intermediary range is characterised by the signal transitioning into a well-defined, single peak. The intensities range from 1.5 to 1.9, with the exception of 1.55, which yields an energy resolution above 100%. The energy resolutions specific to this region are between 10% to 100%.

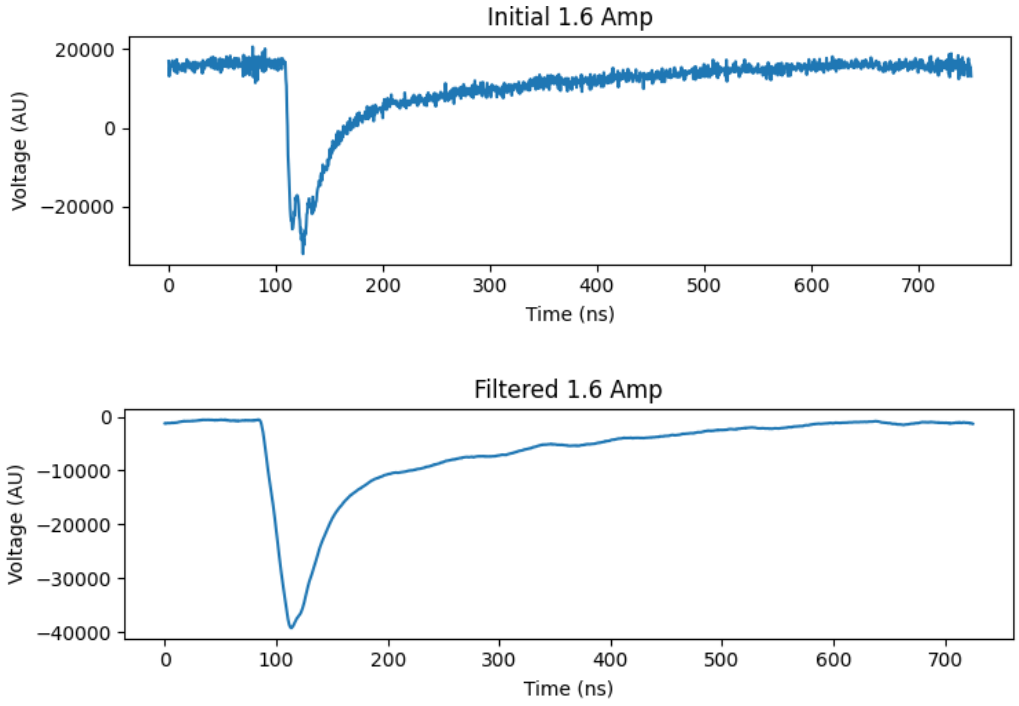

Figure 15: Raw and Filtered Waveform at 1.6 Intensity

Looking at the Initial waveform at 1.6 intensity in figure 15, the noise is still present, but it varies much less than the total peak value. The filtered waveform starts very close to 0. This suggests that the algorithm performs better, being more robust for increasingly stronger signals. The filtered waveform also retains the global feature of a well-defined peak. This might suggest that the single peaks present in the previous regime are stacking up due to the linear nature of the single cell signals.

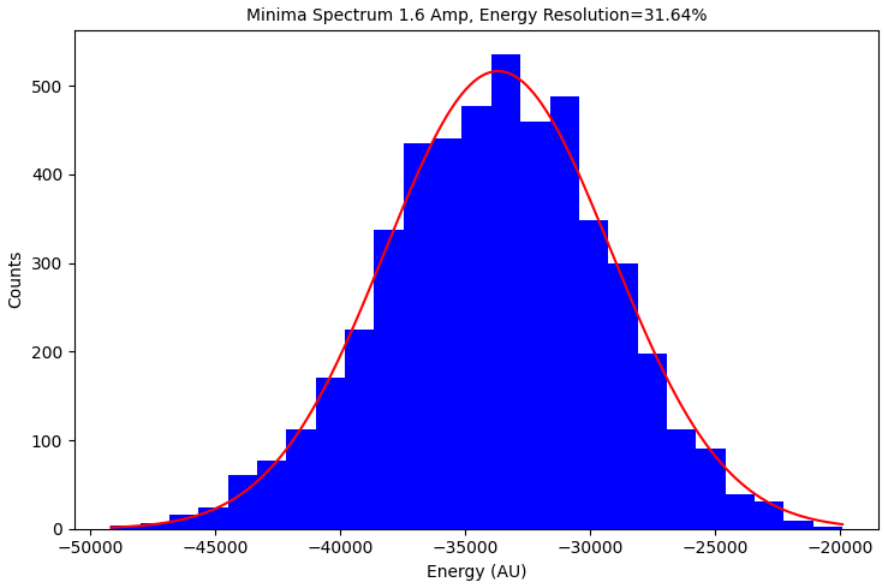

Figure 16: Gaussian Fit of 1.5 Intensity Spectrum

The mean of the Gaussian present in figure 16 is significantly farther away from 0 compared to the

previous Low Intensity measurement. This is a general trend in the Intermediary mode. This confirms that the signal is well-differentiated from noise and it gets more accurate as the intensity is increased. This is seen in the value of the energy resolution which is $E_{res} = 31.64\%$. The general trend seems to be that the peak smooths out, visible in the raw signal as well.

4.2.3 High Intensity

The best waveforms in terms of shape and energy resolution are found in the intensity range above 1.9, in which the energy resolution is less equal to 10%.

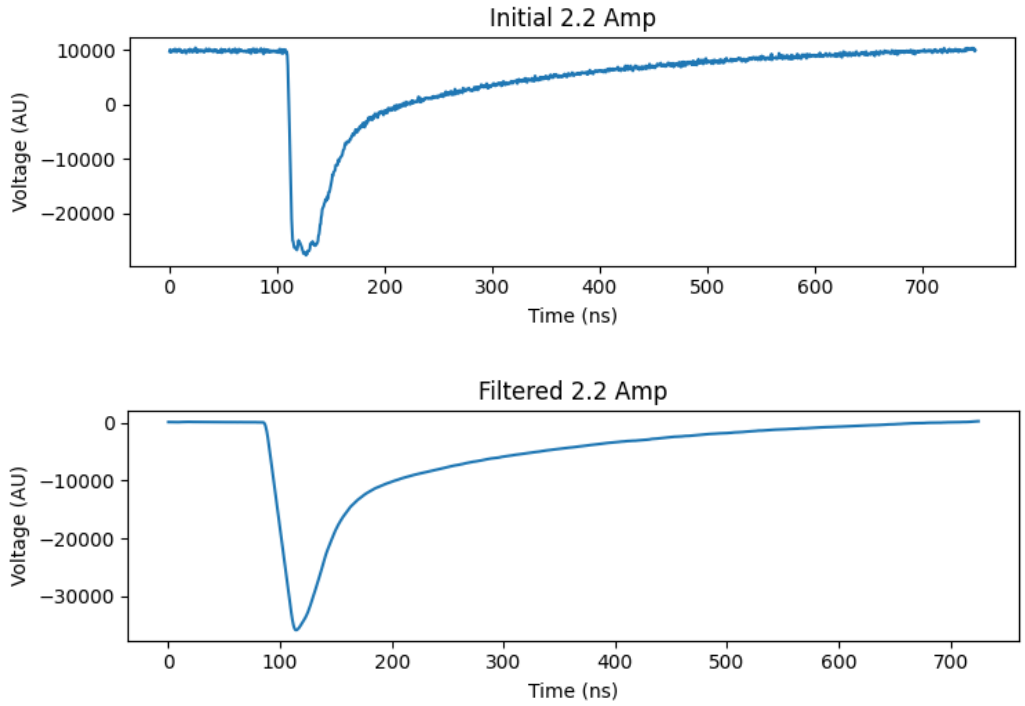

Figure 17: Raw and Filtered Waveform at 2.2 Intensity

Observing figure 18, it is noticeable that the peak tends to smooth out. Any measurements above this intensity yield a saturated signal, which is not of interest in this experiment. The filtering algorithm yields the best-looking waveform, with the start of the signal being extremely close to 0. The signal is very smooth, indicating that noise along the curve is negated.

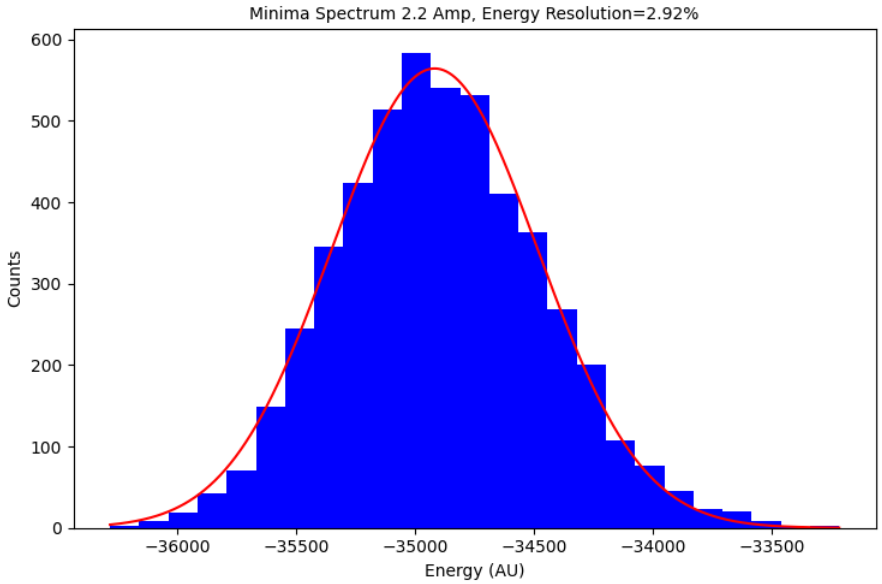

Figure 18: Gaussian Fit of 2.2 Intensity Spectrum

The high intensity regime yields the best energy resolutions up until the saturation point. The best achieved energy resolution for the SiPM is found for an intensity of 2.2, with the energy resolution being $E_{res} = 2.92\%$. A study from 2009 obtained that the energy resolution of a SiPM matrix that operates as a single SiPM to be 20% FWHM at 511 keV [7]. Another study from 2014 determined that the energy resolution of a single SiPM cell in the range of 3 MeV to 5 MeV is 3% to 4% [8]. The result is comparable to other determined values, with the parallel SiPM array at maximum light intensity can achieve a resolution of 2.92%, which is similar to the performance of a single detector.

4.3 Digitizer Simulated Sampling Rates

A fast digitizer with a high acquisition rate or sampling rate is essential in determining the time and energy resolution of a detector. The Acqiris digitizer used in the experiment has a sampling rate of 2 GS/s. This is a large sampling rate and multi-channel devices which have such a sampling rate are expensive. In order to confirm if the SiPM parallel configuration could yield similar or reliable results for other acquisition devices, a simulation was conducted based on the sampling rate. As such, energy resolutions were calculated again from simulated, downsampled data points using moving averages and the Nyquist Theorem.

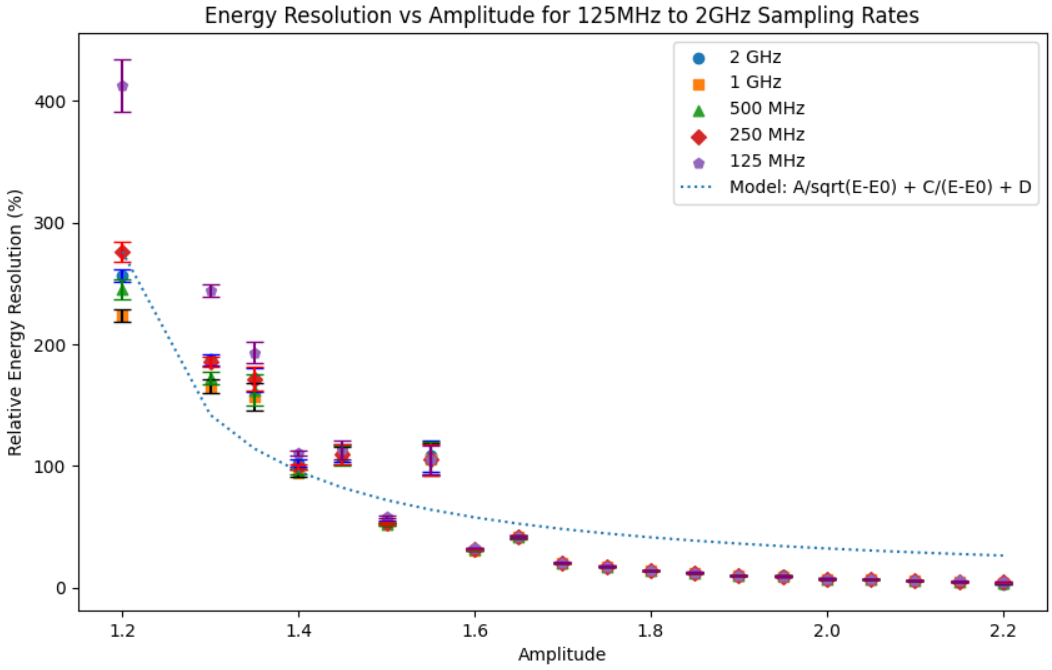

Figure 19: Energy resolutions for simulated downsampled sampling rates

The results for the energy resolutions are presented in figure 19. A proportionality model was fit to the obtained relative energy resolutions. The model is used as a visual confirmation that the general trend is followed by all simulated cases. The model confirms the Poisson nature of the phenomenon. A table containing all the energy resolutions for all cases is presented below in table 1, with red representing the Low Intensity measurements, yellow was used for Intermediary Intensity and finally green for High Intensity.

Amp	2GHz	1GHz	500MHz	250MHz	125MHz
1.2	$256.37 \pm 5.14\%$	$223.84 \pm 5.51\%$	$245.06 \pm 8.29\%$	$276.24 \pm 8.18\%$	$412.69 \pm 21.71\%$
1.3	$187.65 \pm 4.65\%$	$165.62 \pm 5.80\%$	$172.27 \pm 4.82\%$	$185.60 \pm 4.30\%$	$244.31 \pm 5.22\%$
1.35	$171.14 \pm 9.98\%$	$157.08 \pm 11.19\%$	$162.29 \pm 12.71\%$	$171.53 \pm 9.86\%$	$193.17 \pm 8.89\%$
1.4	$102.56 \pm 3.01\%$	$94.27 \pm 2.63\%$	$95.54 \pm 2.08\%$	$99.53 \pm 2.11\%$	$110.62 \pm 2.30\%$
1.45	$111.09 \pm 7.23\%$	$109.01 \pm 7.36\%$	$108.70 \pm 7.91\%$	$110.07 \pm 8.16\%$	$113.36 \pm 7.26\%$
1.5	$54.13 \pm 0.85\%$	$51.99 \pm 1.07\%$	$52.14 \pm 1.13\%$	$52.80 \pm 1.09\%$	$58.07 \pm 0.94\%$
1.55	$108.47 \pm 12.84\%$	$105.54 \pm 13.32\%$	$106.86 \pm 13.15\%$	$105.27 \pm 12.54\%$	$105.16 \pm 12.18\%$
1.6	$31.64 \pm 0.77\%$	$30.72 \pm 0.54\%$	$31.20 \pm 0.35\%$	$31.56 \pm 0.34\%$	$32.66 \pm 0.44\%$
1.65	$41.64 \pm 1.22\%$	$42.00 \pm 1.35\%$	$41.69 \pm 1.39\%$	$41.92 \pm 1.46\%$	$42.09 \pm 1.26\%$
1.7	$20.36 \pm 0.26\%$	$20.28 \pm 0.32\%$	$20.50 \pm 0.20\%$	$20.52 \pm 0.17\%$	$20.74 \pm 0.24\%$
1.75	$17.76 \pm 0.29\%$	$17.48 \pm 0.26\%$	$17.41 \pm 0.27\%$	$17.44 \pm 0.34\%$	$17.66 \pm 0.35\%$
1.8	$13.91 \pm 0.17\%$	$13.91 \pm 0.15\%$	$13.93 \pm 0.18\%$	$13.94 \pm 0.16\%$	$14.03 \pm 0.21\%$
1.85	$12.62 \pm 0.15\%$	$12.40 \pm 0.19\%$	$12.33 \pm 0.24\%$	$12.26 \pm 0.27\%$	$12.49 \pm 0.22\%$
1.9	$10.09 \pm 0.14\%$	$10.13 \pm 0.15\%$	$10.20 \pm 0.16\%$	$10.22 \pm 0.17\%$	$10.21 \pm 0.16\%$
1.95	$9.70 \pm 0.11\%$	$9.53 \pm 0.13\%$	$9.59 \pm 0.11\%$	$9.45 \pm 0.10\%$	$9.49 \pm 0.13\%$
2.0	$7.44 \pm 0.12\%$	$7.40 \pm 0.09\%$	$7.46 \pm 0.12\%$	$7.49 \pm 0.10\%$	$7.47 \pm 0.10\%$
2.05	$7.07 \pm 0.06\%$	$7.09 \pm 0.09\%$	$7.05 \pm 0.05\%$	$6.96 \pm 0.10\%$	$7.07 \pm 0.09\%$
2.1	$5.79 \pm 0.05\%$	$5.85 \pm 0.06\%$	$5.88 \pm 0.13\%$	$6.01 \pm 0.08\%$	$6.11 \pm 0.10\%$
2.15	$4.63 \pm 0.04\%$	$4.99 \pm 0.07\%$	$5.22 \pm 0.04\%$	$5.38 \pm 0.05\%$	$5.47 \pm 0.07\%$
2.2	$2.92 \pm 0.05\%$	$3.72 \pm 0.06\%$	$4.18 \pm 0.05\%$	$4.43 \pm 0.06\%$	$4.56 \pm 0.04\%$

Table 1: Relative Energy Resolutions for original and simulated sampling rates against laser intensity

By comparing across the Low Intensity region, 2 GHz is not the best option. The 1 GHz yields a better energy resolution, with 125 MHz yielding the worst by far. The 1 GHz simulated device mostly outperforms all other devices in the Low Intensity region. This might be due to a lower amount of points which might reduce the noise variance in the Raw waveforms. The 125 MHz simulated device becomes comparable to the other device at an intensity of 1.45.

For the Intermediary region, the measurement at 1.55 intensity yields high errors and a higher than expected value for the resolution. This might originate from an error in the measurement process. Otherwise, the devices share the same order of magnitude in the energy resolutions, as well as in their errors. All devices follow the same trend of converging towards values under 10%.

The High Intensity region presents mixed results, with the 2 GHz device outperforming the rest only for 2.1, 2.15 and 2.2 amplitudes. This is important as these represent the upper intensity limits for a non-saturated signal. This confirms that the best performing device is the 2 GHz Acqiris, but the rest of the simulated devices perform comparably well.

5 Conclusion

An analysis on all the components of the experimental setup described in the paper has been done. The preamplifier, LED Pulser, Digitizer and the Python program all play essential roles in the readout of the signals. The relative energy resolution is studied as the main parameter that needs to be optimized in order to gain insight into the efficiency of a parallel SiPM array.

The Python program performed well for the task of filtering, binning and fitting in the intermediary and high intensity ranges. The lower intensity ranges proved to be trickier to align and analyse due to the noisy behaviour of the signal. This can be improved on in the future through a reassessment of the filtering method.

The Preamplifier is the device mainly responsible for amplifying the signal obtained from the SiPM. It offers a wide range of choice thanks to the adjustable resistance element, as well as 2 channels. Although only one channel was used for the experiment, it can support 2 simultaneous signals as well. The extreme with the highest resistance was chosen, as it offered the best signal-to-noise ratio. This setting ensured that parasitic capacitance effects are minimized, which would have required higher intensities and would have introduced unwanted oscillatory behaviour in the system.

The digitizer is an essential component in the setup as it converts analog signals into digital signals that is then further used for data analysis. The Acqiris DAQ device is capable of handling up to 2 GS/s, with an availability for 4 channel inputs, as well as a trigger input. The digitizer could resolve rather easily the signals in the intermediary and high intensity regions. This raised the question of how other devices might perform. The 1 GHz sampling rate proved to be the best for low intensity measurements, suggesting a good balance between signal integrity and noise reduction. The simulated lower sampling devices maintain a degree of consistency across all ranges.

The parallel SiPM array is characterized in this study by the relative energy resolution. For low intensity measurements, the best resolution was achieved by the simulated 1 GHz device. The 2 GHz device possesses a similar energy resolution in that range. The 2 GHz device makes it possible for Single Cell behaviour to be observed in the low intensity region. This, alongside the model that was fit in Figure 19, confirm the Poisson nature of the parallel configuration, backed up by theory. The Intermediary intensity region, all sampling rates show that the SiPM array maintains consistent, increasingly better performance over the whole range. At high intensities, the 2 GHz device outperforms the rest, suggesting that for high intensity events to be captured accurately, a high sampling rate device is needed, although all other simulated devices performed comparably well.

This research aimed to highlight the critical parameters involved in the optimization of the readout of a SiPM-based detector. The preamplifier settings, the parallel configuration of the SiPMs, the sampling rate and the data processing program all play an essential role in determining the energy resolution of the array. This can set the foundation for further research and innovation in developing compact, efficient and accurate neutron detectors, that are both usable in vacuum and in strong magnetic fields.

As a follow-up, it is important to study the Series configuration of 2 SiPMs in order to shed more light into the advantages and disadvantages of different arrays. By using a well-studied radioactive source, for instance the 511 keV peak of Na22, the energy resolution can be determined and compared to the single SiPM. Addition of a scintillator into the setup would provide additional information into how

the arrays would work in tandem with such a material. This would add a further parameter that can be optimized, for instance the light yield of the material.

Bibliography

[1] P. Buzhan, B. Dolgoshein, L. Filatov, A. Ilyin, V. Kantzerov, V. Kaplin, A. Karakash, F. Kayumov, S. Klemin, E. Popova, and S. Smirnov, "Silicon photomultiplier and its possible applications," *Nuclear Instruments and Methods in Physics Research Section A: Accelerators, Spectrometers, Detectors and Associated Equipment*, vol. 504, no. 1, pp. 48–52, 2003. Proceedings of the 3rd International Conference on New Developments in Photodetection.

[2] "What is an SiPM and how does it work? — Hamamatsu Photonics — hub.hamamatsu.com." https://hub.hamamatsu.com/us/en/technical-notes/mppc-sipms/what-is-an-SiPM-and-how-does-it-work.html. [Accessed 13-07-2024].

[3] O. Girard, G. Haefeli, A. Kuonen, and M. E. Stramaglia, "Silicon photomultiplier multichannel arrays for the lhcb scintillating fibre tracker," in *2017 IEEE Nuclear Science Symposium and Medical Imaging Conference (NSS/MIC)*, pp. 1–3, 2017.

[4] C. Degenhardt, B. Zwaans, T. Frach, and R. de Gruyter, "Arrays of digital silicon photomultipliers — intrinsic performance and application to scintillator readout," in *IEEE Nuclear Science Symposuim Medical Imaging Conference*, pp. 1954–1956, 2010.

[5] S. Tavernier, *Experimental Techniques in Nuclear and Particle Physics*. Springer, 2 2010.

[6] S. Seifert, H. T. van Dam, J. Huizenga, R. Vinke, P. Dendooven, H. Lohner, and D. R. Schaart, "Simulation of silicon photomultiplier signals," *IEEE Transactions on Nuclear Science*, vol. 56, no. 6, pp. 3726–3733, 2009.

[7] G. Llosa, N. Belcari, M. Giuseppina, G. Collazuol, S. Marcatili, S. Moehrs, F. Morsani, C. Piemonte, and A. Del Guerra, "Energy and timing resolution studies with silicon photomultipliers (sipms) and 4-pixel sipm matrices for pet," *Nuclear Science, IEEE Transactions on*, vol. 56, pp. 543 – 548, 07 2009.

[8] M. Nocente, A. Fazzi, M. Tardocchi, C. Cazzaniga, M. Lorenzoli, C. Pirovano, M. Rebai, C. Uboldi, V. Varoli, and G. Gorini, "Experimental investigation of silicon photomultipliers as compact light readout systems for gamma-ray spectroscopy applications in fusion plasmasa)," *Review of Scientific Instruments*, vol. 85, p. 11E108, 07 2014.

Appendices

A Full results

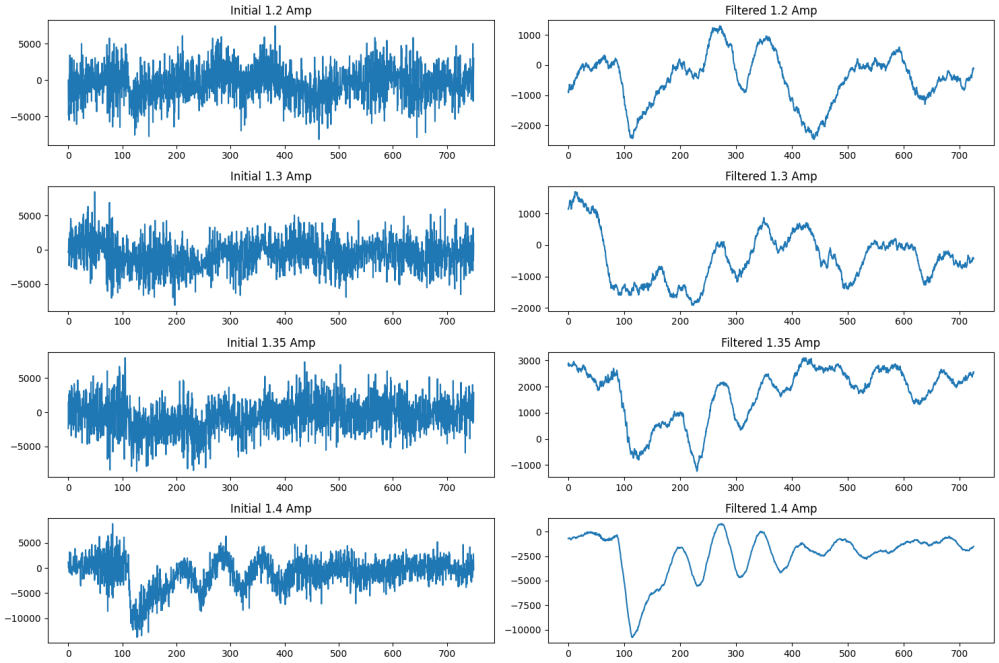

Figure 20: Low Intensity Measurement

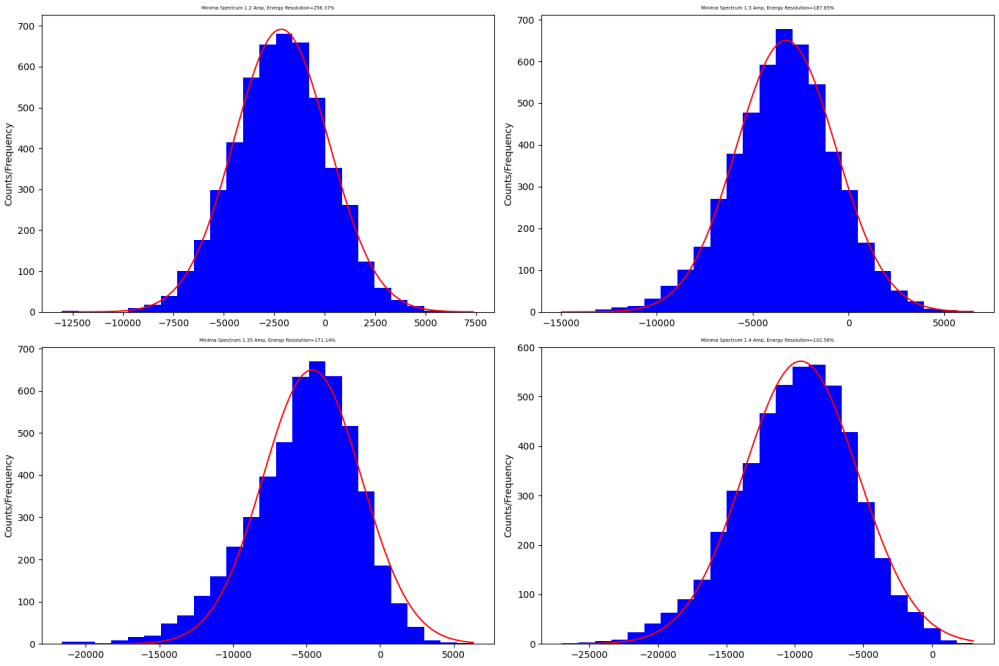

Figure 21: Low Intensity Gaussians

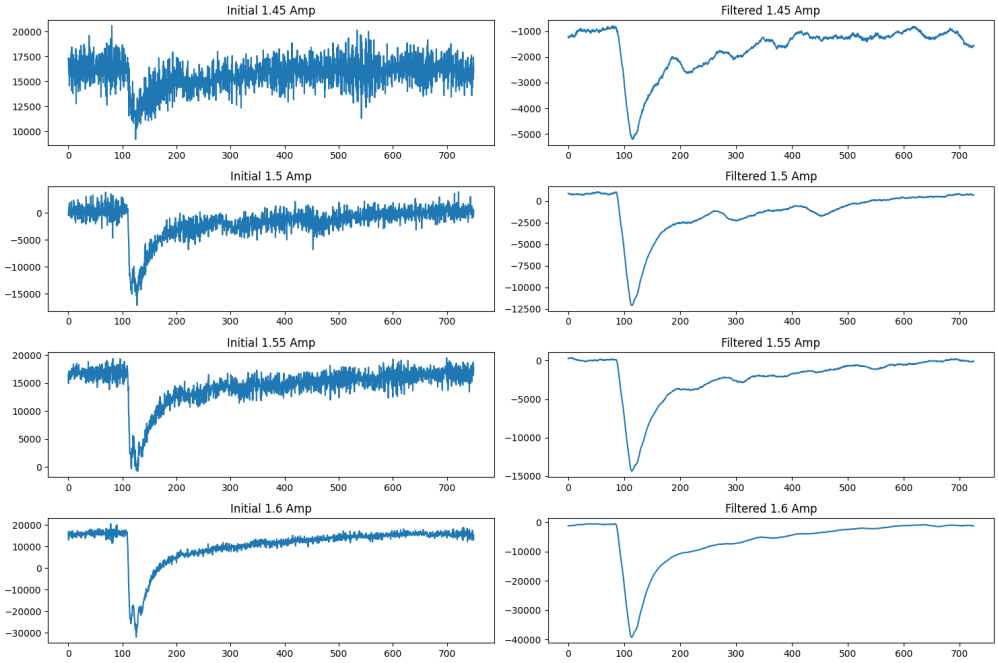

Figure 22: Intermediary Intensity Measurement

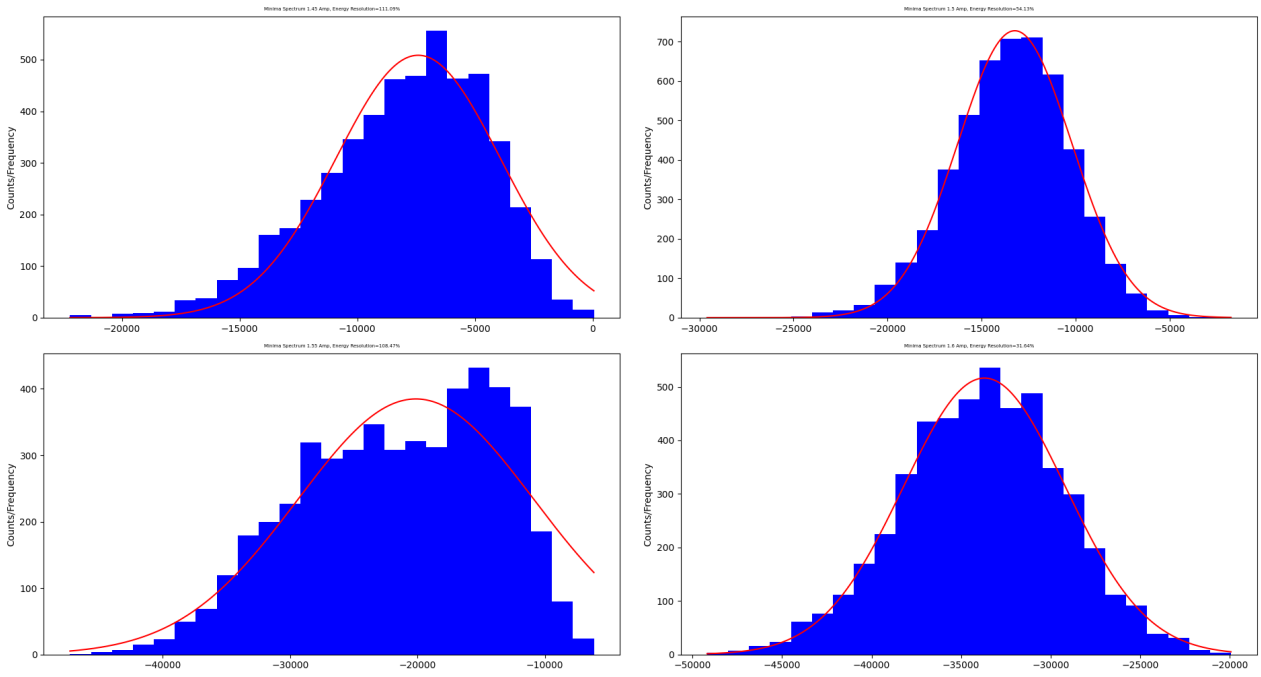

Figure 23: Intermediary Intensity Gaussian

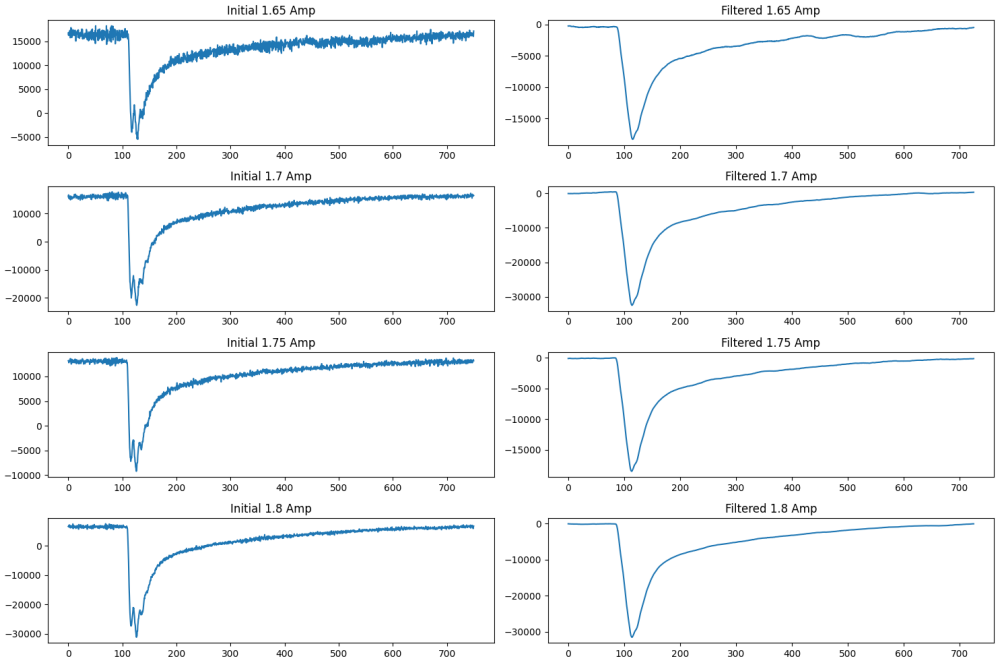

Figure 24: Intermediary and High Intensity Measurement

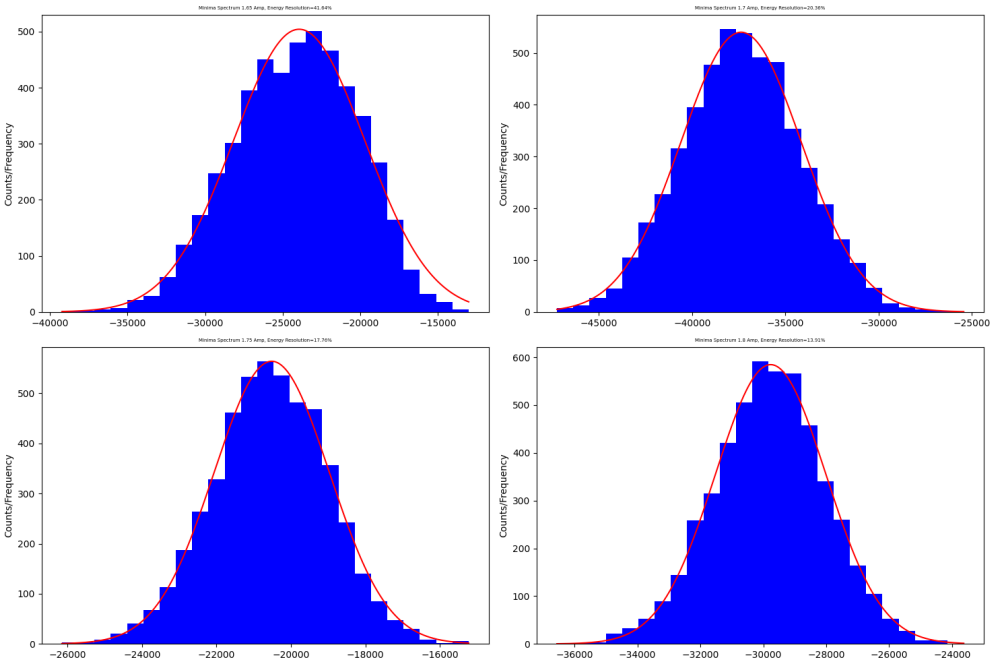

Figure 25: Intermediary and High Intensity Measurement

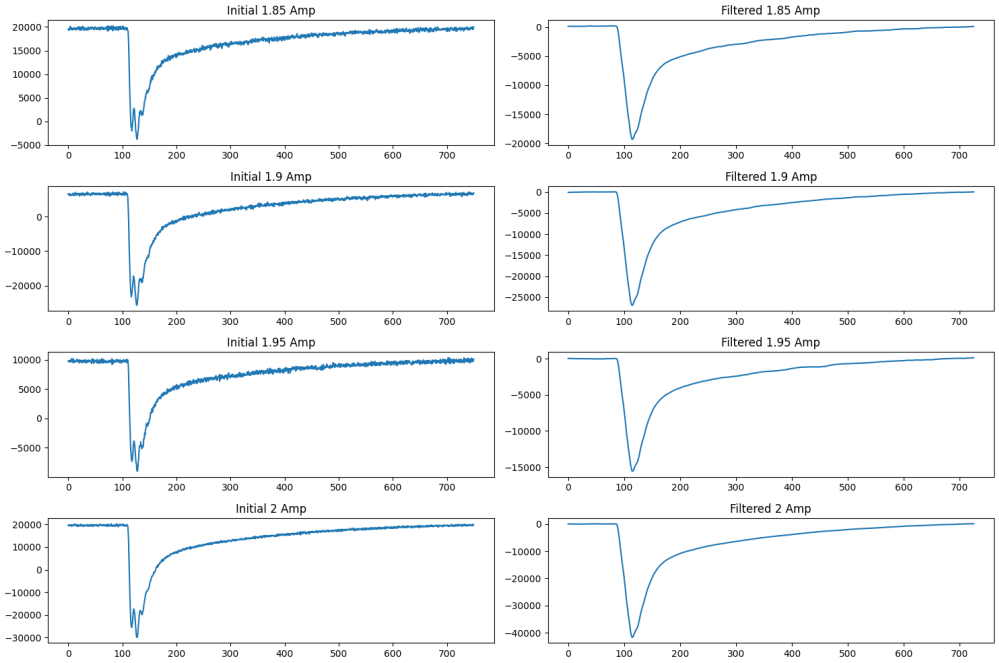

Figure 26: High Intensity Measurement

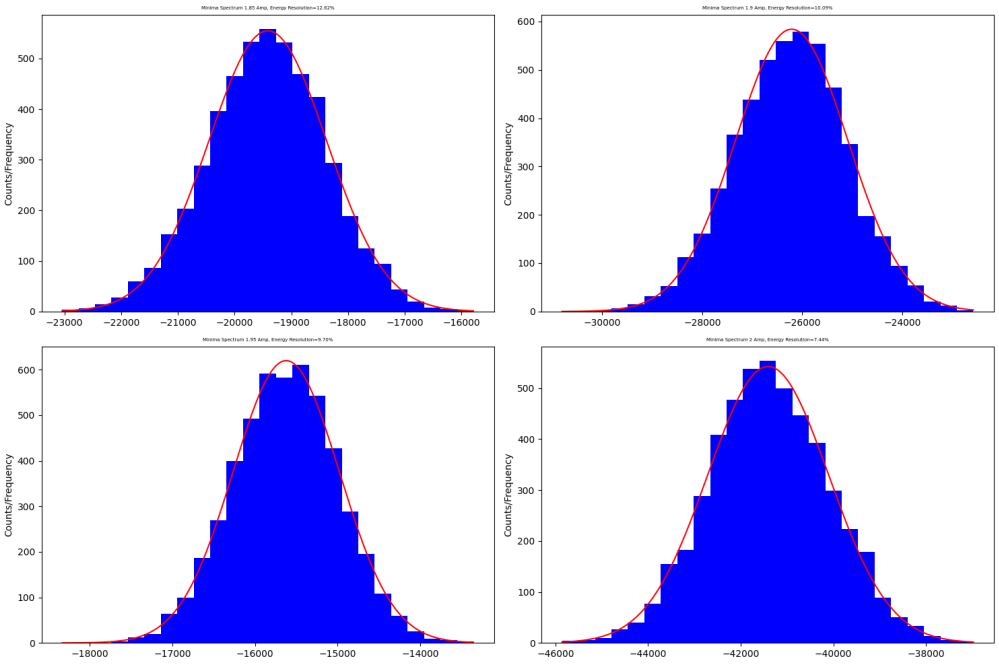

Figure 27: Intermediary and High Intensity Measurement

B Gaussian parameters and errors

Errors were calculated from μ and σ and their corresponding errors. The Energy resolution errors were found as:

$$\Delta E_{res} = |E_{res}| \sqrt{(\frac{\Delta\mu}{\mu})^2 + (\frac{\Delta\sigma}{\sigma})^2 + 2\frac{\Delta\mu\Delta\sigma}{\mu\sigma}} \tag{9}$$

Data Set	R^2(%)	mu	sigma	Mu Error	Sigma Error
1.2 Amp	99.8285	-2160.0495	2351.4661	22.5904	22.5904
1.3 Amp	99.6271	-3259.0983	2596.8317	35.8321	35.8324
1.35 Amp	97.7859	-4615.3901	3354.0250	113.2625	113.2842
1.4 Amp	99.0980	-9570.3105	4167.9902	85.0584	85.1221
1.45 Amp	95.5875	-7411.6834	3496.1025	151.8602	155.9131
1.5 Amp	99.7083	-13227.8647	3040.1968	38.7024	38.7026
1.55 Amp	85.0337	-20124.2587	9269.2193	701.5099	774.5329
1.6 Amp	98.8825	-33698.2632	4526.8272	97.6693	97.7430
1.65 Amp	98.5240	-23937.5547	4232.3548	104.8798	105.4690
1.7 Amp	99.6761	-37374.3267	3230.7321	38.4072	38.4319
1.75 Amp	99.4961	-20517.4039	1547.4151	23.4603	23.4627
1.8 Amp	99.7008	-29765.7644	1757.8022	20.8306	20.8317
1.85 Amp	99.7238	-19415.3812	1040.1240	11.5422	11.5435
1.9 Amp	99.5976	-26211.4843	1123.3430	15.4616	15.4652
1.95 Amp	99.7668	-15622.3647	643.2037	6.9232	6.9235
2 Amp	99.4742	-41409.1578	1307.7880	19.8485	19.8523
2.05 Amp	99.8479	-23508.3227	705.4044	6.1740	6.1741
2.1 Amp	99.8030	-28355.5593	697.5422	6.3658	6.3677
2.15 Amp	99.8202	-31720.8414	623.1531	5.6938	5.6942
2.2 Amp	99.4706	-34917.3436	432.9017	6.7228	6.7254

Figure 28: 2 GHz data

Data Set	R^2(%)	mu	sigma	Mu Error	Sigma Error
1.2 Amp	99.6948	-1630.3636	1559.9201	19.6166	19.6167
1.3 Amp	99.2025	-2577.5703	1826.5020	37.4141	37.4143
1.35 Amp	96.5644	-3758.4342	2507.8185	107.0810	107.1957
1.4 Amp	99.1758	-8011.2513	3210.5555	63.9463	63.9769
1.45 Amp	95.4529	-6136.1583	2840.1497	128.5914	132.2948
1.5 Amp	99.4571	-10924.8596	2420.0319	40.7587	40.7807
1.55 Amp	83.7220	-16656.5323	7482.7661	617.5939	667.2254
1.6 Amp	99.4236	-27671.0580	3622.6663	56.7790	56.8175
1.65 Amp	98.2541	-19542.4413	3485.3232	94.8390	95.3836
1.7 Amp	99.5210	-30556.6506	2636.9630	38.0318	38.0417
1.75 Amp	99.5869	-16683.8436	1242.2507	16.9275	16.9294
1.8 Amp	99.7929	-24224.9631	1439.0642	14.3890	14.3893
1.85 Amp	99.5490	-15730.1489	828.5247	11.9146	11.9154
1.9 Amp	99.5765	-21246.8870	912.9425	12.6953	12.7004
1.95 Amp	99.6384	-12640.0478	511.0961	6.8652	6.8656
2 Amp	99.6853	-33640.5954	1056.2571	12.4327	12.4347
2.05 Amp	99.7046	-19027.2553	573.5456	7.0338	7.0338
2.1 Amp	99.7231	-23021.9531	571.4195	6.0316	6.0351
2.15 Amp	99.5546	-25885.0706	548.6735	7.8468	7.8481
2.2 Amp	99.4083	-29011.3123	460.2935	7.7339	7.7341

Figure 29: 1 GHz data

Data Set	R^2(%)	mu	sigma	Mu Error	Sigma Error
1.2 Amp	99.4365	-1159.6051	1206.6882	20.0140	20.0145
1.3 Amp	99.4980	-1922.0121	1406.0033	22.7027	22.7028
1.35 Amp	95.8993	-2697.2525	1858.7684	86.0953	86.2147
1.4 Amp	99.4987	-5776.8740	2343.7379	36.3654	36.3712
1.45 Amp	94.5266	-4373.0562	2018.5669	99.3633	100.9288
1.5 Amp	99.3974	-7794.0272	1725.6951	30.5156	30.5347
1.55 Amp	85.6659	-11797.6935	5353.4120	425.3591	465.6235
1.6 Amp	99.7846	-19707.6387	2610.9774	25.5666	25.5781
1.65 Amp	98.1095	-13881.4544	2457.1806	69.5003	69.7817
1.7 Amp	99.8296	-21691.9942	1888.0944	16.5737	16.5756
1.75 Amp	99.5418	-11818.6466	873.7237	12.7503	12.7511
1.8 Amp	99.6969	-17119.8241	1012.3902	12.3009	12.3011
1.85 Amp	99.3073	-11102.7123	581.2222	10.5677	10.5681
1.9 Amp	99.4855	-14953.0857	647.6502	9.7521	9.7618
1.95 Amp	99.7351	-8910.4082	362.7362	4.0618	4.0626
2 Amp	99.4397	-23668.2105	749.8127	12.1237	12.1242
2.05 Amp	99.9167	-13369.9576	400.1377	2.6059	2.6059
2.1 Amp	98.8889	-16184.3074	403.9291	8.8333	8.8352
2.15 Amp	99.8483	-18228.5307	403.6689	3.3274	3.3280
2.2 Amp	99.7128	-20623.0965	366.0614	4.3170	4.3171

Figure 30: 500 MHz data

Data Set	R^2(%)	mu	sigma	Mu Error	Sigma Error
1.2 Amp	99.6553	-842.9332	988.7500	13.4774	13.4774
1.3 Amp	99.6898	-1387.5764	1093.5652	14.1806	14.1806
1.35 Amp	98.0188	-1950.9205	1420.9742	47.2596	47.2605
1.4 Amp	99.5754	-4039.7793	1707.2576	25.4395	25.4411
1.45 Amp	94.6008	-3009.8373	1406.7028	69.8638	71.6227
1.5 Amp	99.4764	-5391.8146	1208.8806	20.3694	20.3761
1.55 Amp	86.7659	-8109.2853	3624.7800	282.0489	305.8894
1.6 Amp	99.7956	-13505.7380	1810.1085	17.2833	17.2918
1.65 Amp	97.9904	-9496.6106	1690.4295	49.8266	50.0209
1.7 Amp	99.8828	-14810.1864	1290.2555	9.5735	9.5742
1.75 Amp	99.2499	-8058.3655	596.6481	10.7969	10.7996
1.8 Amp	99.7756	-11650.5263	689.7528	7.2710	7.2711
1.85 Amp	99.0919	-7534.5404	392.3426	8.2947	8.2948
1.9 Amp	99.3855	-10129.4557	439.5474	7.0973	7.1061
1.95 Amp	99.7767	-6035.1822	242.2270	2.5053	2.5054
2 Amp	99.6329	-15976.4457	507.8991	6.6188	6.6193
2.05 Amp	99.5948	-9028.2400	266.7175	3.7264	3.7268
2.1 Amp	99.5997	-10924.1410	278.9190	3.7468	3.7474
2.15 Amp	99.8139	-12312.5555	281.2495	2.6180	2.6183
2.2 Amp	99.6671	-14000.0172	263.3336	3.3286	3.3289

Figure 31: 250 MHz data

Data Set	R^2(%)	mu	sigma	Mu Error	Sigma Error
1.2 Amp	99.3436	-494.3763	866.3370	16.5595	16.5595
1.3 Amp	99.7816	-892.5446	925.9322	9.7027	9.7027
1.35 Amp	98.8812	-1294.2859	1061.6308	26.8285	26.8285
1.4 Amp	99.6295	-2644.9307	1242.3516	17.5701	17.5701
1.45 Amp	95.8167	-1932.9226	930.4367	39.8837	40.3824
1.5 Amp	99.6982	-3437.2197	847.5291	10.9753	10.9755
1.55 Amp	87.7087	-5125.1684	2288.5978	173.7068	187.4029
1.6 Amp	99.6919	-8543.7964	1184.9044	14.1544	14.1559
1.65 Amp	98.5210	-5988.9615	1070.4428	27.1253	27.1841
1.7 Amp	99.7497	-9326.0074	821.1855	8.8909	8.8915
1.75 Amp	99.2355	-5066.2233	379.8282	7.0620	7.0630
1.8 Amp	99.5647	-7306.6763	435.2933	6.2404	6.2406
1.85 Amp	99.5086	-4721.3450	250.4395	4.1945	4.1945
1.9 Amp	99.4940	-6328.3376	274.4228	4.1575	4.1594
1.95 Amp	99.6397	-3772.0471	152.0815	1.9901	1.9903
2 Amp	99.6632	-9954.6472	315.6752	3.9268	3.9270
2.05 Amp	99.6926	-5620.0288	168.6745	2.0286	2.0289
2.1 Amp	99.4180	-6794.3818	176.2255	2.8460	2.8468
2.15 Amp	99.6879	-7661.1185	177.8589	2.1252	2.1254
2.2 Amp	99.8620	-8728.4961	168.9338	1.4061	1.4061

Figure 32: 125 MHz data